Biochemistry and Biophysics Reports 42 (2025) 102026

Contents lists available at ScienceDirect

Biochemistry and Biophysics Reports

journal homepage: www.elsevier.com/locate/bbrep

High-resolution transcriptome analysis on a mouse model of neonatal hypoxic-ischemic encephalopathy using single-nucleus RNA-seq

Nao Wakui [a], Takashi Shimbo [b,c,*], Morifumi Hanawa [d], Tomomi Kitayama [c,d], Yukari Yamamoto [c,d], Yuya Ouchi [c,d], Kotaro Saga [b], Aiko Okada [a], Kazuya Mimura [a], Katsuto Tamai [b,d], Masayuki Endo [a,c,e]

[a] Department of Obstetrics and Gynecology, Graduate School of Medicine, Osaka University, Suita, Japan
[b] Department of Stem Cell Therapy Science, Graduate School of Medicine, Osaka University, Suita, Japan
[c] StemRIM Institute of Regeneration-Inducing Medicine, Osaka University, Suita, Osaka, Japan
[d] StemRIM Inc., Ibaraki, Osaka, Japan
[e] Department of Children's and Women's Health, Division of Health Science, Graduate School of Medicine, Osaka University, Suita, Osaka, Japan

ARTICLE INFO

Keywords:
Neonatal hypoxic-ischemic encephalopathy
Mouse model
Single-nucleus RNA sequencing
Neuronal damage
Hippocampus
Interferon activation

ABSTRACT

Neonatal hypoxic-ischemic encephalopathy (HIE) encompasses brain injuries resulting from dysregulated oxygen or blood flow to the brain before, during, or immediately after birth. During the acute phase, neuronal damage is driven by excitotoxicity, with permanent injury manifesting over the subsequent hours. Treatment options have limited efficacy, requiring deeper insights into HIE pathogenesis. Recent advances in single-cell RNA sequencing have enabled molecular investigations of diverse diseases. However, the large size of certain cells, such as neurons, has posed challenges in studying conditions where neuronal damage is central. Thus, we employed single-nucleus RNA sequencing to evaluate damages in a mouse model of HIE and found pronounced changes in the hippocampus with significantly reduced neuronal populations. We observed the characteristic activation of hippocampal microglia, confirmed by immunostaining in the HIE model. These alterations were specific to combined hypoxic-ischemic conditions and were not observed with hypoxia or ischemia alone. These findings provide insights into the molecular and anatomical impact of HIE and highlight the hippocampus as a critical focus for understanding disease mechanisms and therapeutic development.

1. Introduction

Neonatal hypoxic-ischemic encephalopathy (HIE) is a spectrum of brain injuries occurring before, during, or shortly after birth due to reduced or interrupted brain oxygen or blood flow [1]. HIE often results in severe, long-term neurological complications, including cerebral palsy, epilepsy, and developmental disorders affecting motor neurons. Its incidence varies significantly, ranging from 1 to 8 per 1000 live births in developed countries and up to 26 per 1000 live births in developing countries [2]. Globally, HIE directly contributes to 23–25 % of neonatal deaths [3]. While therapeutic hypothermia is the current standard of care for neonates with HIE, its efficacy is limited, necessitating the development of novel and effective treatments.

The acute phase of HIE involves hypoxia and ischemia, which reduce oxygen and glucose supply to the brain, leading to neuronal and membrane damage. Hours after the initial insult, mitochondrial dysfunction exacerbates damage by generating free radicals such as reactive oxygen and nitrogen species, culminating in progressive neuronal necrosis and apoptosis. Once intracellular Ca^{2+} concentration reaches a plateau, neuronal damage becomes irreversible—a phenomenon known as secondary neuronal cell death [4]. Despite significant advances in understanding the biochemical cascades of HIE, many aspects of its pathology remain unclear.

Advances in transcriptomics, particularly single-cell RNA sequencing (scRNA-seq), have provided detailed insights into the molecular mechanisms of various diseases. In mouse models of HIE, scRNA-seq has been instrumental in identifying microglia activation as a key pathological feature [5,6]. However, neurons, the pathogenic centers of HIE, cannot be efficiently analyzed by scRNA-seq due to their large size [7]. Nevertheless, snRNA-seq overcomes this limitation by isolating nuclei and analyzing their RNA content, thereby eliminating cell-size biases inherent in scRNA-seq. Here, we aimed to investigate the damage in a

* Corresponding author. StemRIM Institute of Regeneration-Inducing Medicine, Osaka University, Yamadaoka 2-8, Suita, Osaka, 565-0871, Japan.
E-mail address: shimbot@sts.med.osaka-u.ac.jp (T. Shimbo).

https://doi.org/10.1016/j.bbrep.2025.102026
Received 15 January 2025; Received in revised form 2 April 2025; Accepted 21 April 2025

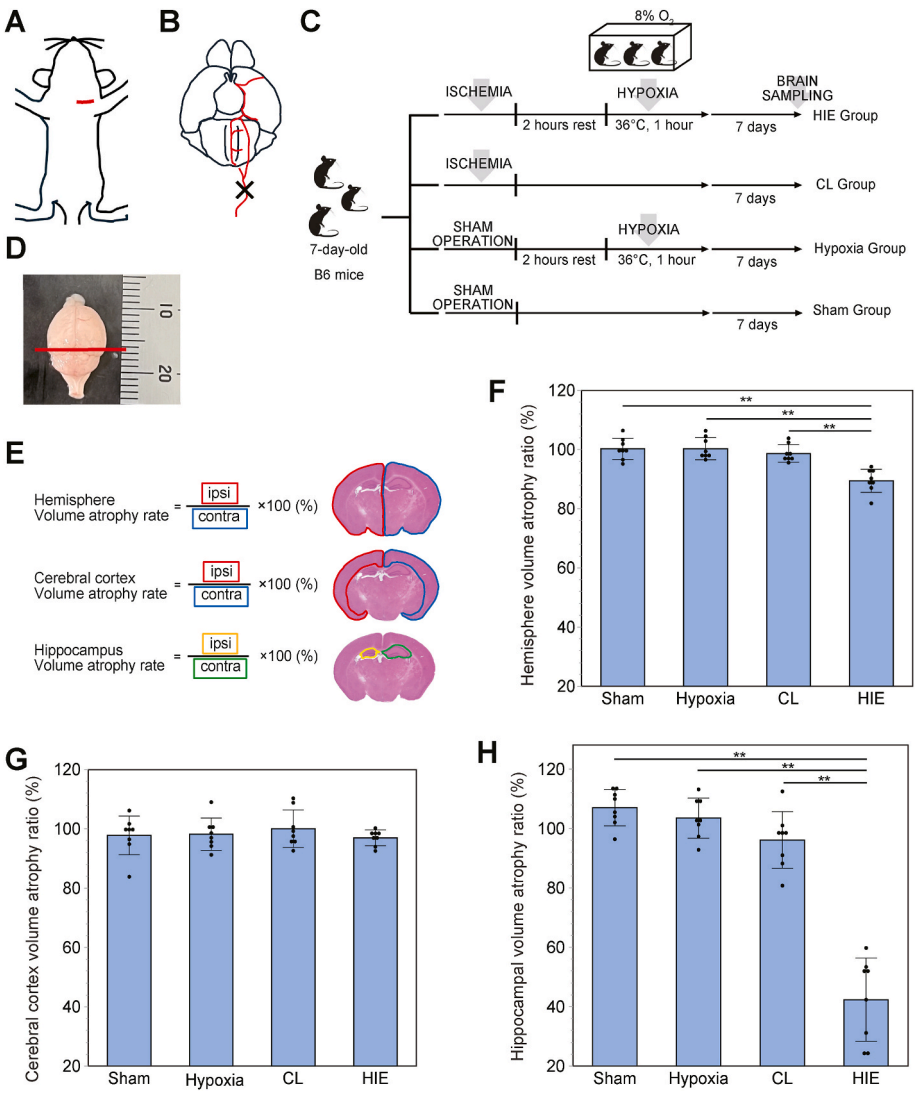

Fig. 1. Procedures for creating an HIE neonatal mouse model
(A) Under sedation with isoflurane, expanding the field of view of the left common carotid artery (CCA) of a P7 mouse.
(B) Left CCA ligated with 6-0 silk.
(C) Timeline for the experiments. Four experimental groups were established by combining ligation and hypoxia conditions.
(D) Location of brain sections (at Bregma-1.5 mm)
(E) Volume atrophy calculation ratios of each region.
Each group contained four males and four females.
(F)Hemisphere volume atrophy ratio. **p < 0.0001. Error bars show means + SD
(G)Cerebral cortex volume atrophy ratio. **p < 0.0001. Error bars show means + SD
(H)Hippocampal atrophy ratio. **p < 0.0001. Error bars show means + SD.

mouse model of HIE using snRNA-seq, enabling the successful profiling of single-cell level transcriptomes and revealing heterogeneity in neuronal impairment across different anatomical brain regions.

2. Methods

2.1. Animal models

All animal procedures were approved by the animal ethics committees of Osaka University Graduate School of Medicine (Approval Number: 02-071-009) and adhered to the ARRIVE guidelines. Pregnant C57BL/6JJcl mice (gestation days E14–E15) were purchased from CLEA Japan (Tokyo, Japan). All mice were housed individually in standard cages under a 12-h light-dark cycle with unrestricted access to food and water.

On postnatal day 7 (P7), male and female pups were randomly assigned to four experimental groups: unilateral carotid ligation followed by hypoxic exposure (HIE group), unilateral carotid ligation only (CL group), sham operation followed by hypoxic exposure (Hypoxia group), and sham operation only (Sham group), involving isolation and threading of the left common carotid artery (CCA) without ligation.

The HIE procedure was adapted from the Rice–Vannucci rat model [8]. P7 mice were anesthetized with isoflurane (3 % for induction, 2 % for maintenance) before permanent ligation of the left CCA 6-0 silk sutures under a stereomicroscope (Fig. 1A and B). Anesthesia duration was limited to under 5 min per pup. After the procedure, pups were returned to their dams for a 2-h recovery period. They were then placed in a chamber maintained at 36 °C using a water bath and perfused with a humidified mixture of 8.0 % oxygen and nitrogen for 1 h. After hypoxic exposure, the pups were returned to their mothers for normal rearing.

For the CL group, the left CCA was ligated without hypoxic exposure. For the Sham group, pups underwent the same anesthesia and surgical exposure as the HIE group, but the CCA was only threaded without ligation of the CCA. Pups in the hypoxia group were subjected to the hypoxia chamber protocol following a sham operation. Each experimental group contained equal numbers of male and female pups (Fig. 1C).

2.2. Hematoxylin and eosin (HE) and immunofluorescence staining

One week after the intervention, the mice were anesthetized and perfused transcardially with 4 % paraformaldehyde (PFA) in 1/15 mol/L phosphate buffer (PB). Brain tissues were carefully isolated and post-fixed in 4 % PFA overnight at 4 °C. The tissues were then bisected at the bregma position and immersed sequentially in a PB solution containing 15 % and 30 % sucrose at 4 °C for cryoprotection. Following cryoprotection, the tissues were embedded in an optimal cutting temperature compound and frozen in liquid nitrogen.

Frozen brain blocks were sectioned into 20-μm slices using a Leica CM3050S cryostat at the bregma −1.5 mm position (Fig. 1D). The sections were stored at −80 °C until further analysis.

For HE staining, sections were dipped in Mayer's hemalum solution (MERCK, 109249) for 5 min, rinsed under running water for 5 min, dipped in 1 % Eosin Y Solution (Wako, 051–06515) for 15 s, and rinsed in pure water. The sections were further washed with anhydrous ethanol (thrice for 2 min) and xylene (thrice for 3 min).

All steps of immunostaining were performed following standard protocols. Briefly, sections were blocked for 1 h with 3.0 % normal goat serum, 0.3 % Triton X-100 in Phosphate-buffered saline (PBS) and incubated with the primary antibody, rabbit anti-Iba1 (1:1000, Wako, 019–19741), in a humidified chamber overnight at 4 °C. The following day, they were rinsed three times in PBS and incubated with a secondary antibody, Alexa Fluor 488-labeled goat anti-rabbit IgG (1:500, abcam), for 1 h at room temperature, and rinsed three times in PBS.

2.3. Calculation of brain atrophy ratio/Iba-1 positive area ratio

To quantify brain volume reduction, whole-brain images were generated by tiling HE-stained sections using an All-in-one Fluorescence Microscope BZ-X700 (KEYENCE). Following the guide described in "The Mouse Brain in Sterotaxic Coordinates [9]," the regions of the ipsilesional hemisphere, cerebral cortex, and hippocampus were marked and compared with those of the contralesional side using Adobe Photoshop 2024 software (Fig. 1E).

In addition, three consecutive sections were prepared at Bregma-1.5 mm per individual, immunostained, and images were combined so that the entire hippocampus was depicted in each section using the same microscope. We used Fiji [10] to measure the Iba-1 positive area of the unilateral hippocampus and calculated it as a percentage of the total area of the ipsilateral hippocampus. The ratio of the percentage area of Iba-1-positive cells in the affected hippocampus to that in the healthy side was determined, and the values of the three intercepts were averaged to obtain the measurements for the individual.

2.4. Brain isolation and nuclei isolation for snRNA-seq

Brains were collected from two male and two female mice in each group on postnatal day 14 (P14). The cerebral cortex and hippocampus were immediately frozen in liquid nitrogen.

The nuclei were isolated following previously described methods [11]. Cortical tissues from each group were pooled and crushed on dry ice. Crushed tissues were resuspended in 5 mL of lysis buffer. The mixture was incubated on ice for 5 min, and the suspension was filtered through a 40-μm cell strainer. A third of the filtered solution was transferred to a new tube and centrifuged at 500×*g* for 5 min at 4 °C. The pellet was resuspended in 1550 μL of wash buffer containing 1 % BSA and 0.2 U/μL recombinant RNase Inhibitor.

Subsequently, 450 μL of Debris Removal Solution (Miltenyi Biotec) was added and gently mixed. To separate nuclear and debris layers, the mixture was layered over 2 mL of 1 × PBS in a 5-mL tube and centrifuged at 2580×*g* for 10 min at 4 °C. The debris layer was washed with nuclei buffer. The nuclei pellet was resuspended in 0.5 mL of nuclei buffer supplemented with 0.2 U/μL recombinant RNase inhibitor. Fixation was performed by adding 2 mL of cold methanol containing 1.25 mg/mL DSP (Thermo Fisher Scientific) dropwise. After 15 min of incubation on ice, methanol was removed via centrifugation at 500×*g* for 5 min at 4 °C. The nuclei were washed twice with nuclei buffer, resuspended in an appropriate volume of nuclei buffer, and passed through a 20-μm filter to obtain a fixed nuclei suspension.

Hippocampal tissues were pooled per group and homogenized. To initiate nuclei isolation, 200 μL of lysis buffer was added, and the tissue was disrupted. An additional 300 μL of lysis buffer was added, and the homogenate was further processed by pipetting. The suspension was passed through a 40-μm cell strainer. Debris removal and methanol fixation were conducted as described for cortical tissues, yielding a fixed nuclear suspension.

2.5. Library preparation for snRNA-seq

Library preparation followed a previously described method [12]. A detailed protocol is provided in Appendix A.

3. Bioinformatics

Sequencing outputs were demultiplexed using BCL Convert (version 4.1.7) [https://jp.support.illumina.com/sequencing/sequencing_software/bcl-convert/downloads.html] with default settings. Index 2 was converted to the unique molecular identifiers, which were manually checked and corrected to match cell barcodes. The FASTQ files were aligned to the mouse reference genome (mm10) using STAR (version 2.7.6a) [13] with the Solo options. The resulting STAR output matrices were filtered based on transcripts gene counts and the percentage of mitochondrial gene content.

Subsequent analyses, including data normalization, scaling, and clustering, were conducted using the Seurat R package (version 5.0.3) [14]. Cell clusters were manually curated using marker genes for identification. Differential gene expression analysis was performed in Seurat with the test.use = "MAST" option. Gene Ontology (GO) enrichment analysis was performed and visualized using the ClusterProfiler package [15,16] and enrichplot tools [17]. Additional data visualization was carried out using the Plotly package (https://plotly.com/).

4. Statistical analysis

Data are presented as mean ± standard deviation (SD). The normality of data distribution was assessed using the Shapiro–Wilk normality test. For comparisons between the four groups with normally distributed data, analysis of variance was performed as a parametric analysis, and the Tukey–Kramer test was conducted for each between-group comparison. Statistical significance was set at $P < 0.05$. All statistical analyses were conducted using JMP Pro 17 software (SAS Institute, Cary, NC, US).

5. Results

We utilized a well-established HIE mouse model [18]. Briefly, mice were anesthetized using isoflurane, followed by permanent ligation of the left common carotid artery. Then, they were exposed to a hypoxic environment consisting of 8 % oxygen and 92 % nitrogen at 36 °C for 1 h. In addition to the HIE group, three control groups were included: a group that underwent left common carotid ligation only (CL group), one subjected to sham surgery and hypoxic exposure (hypoxia group), and

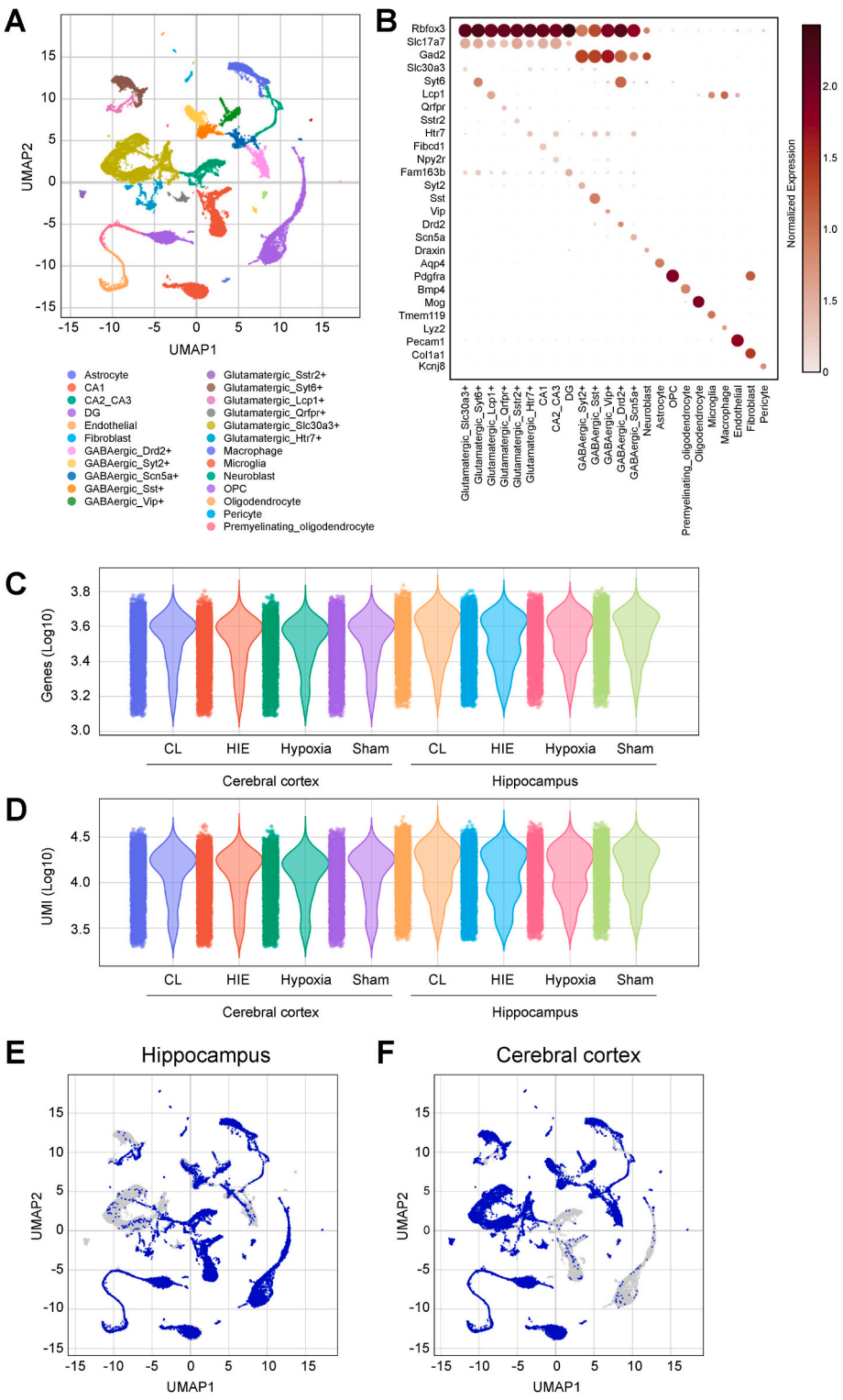

Fig. 2. Single-nucleus RNA-seq on brains including cerebral cortex and hippocampus.
(A) UMAP plot of all snRNA-seq data containing cortex and hippocampus.
(B) Marker genes for each cluster. Dot size represents the percentage of cells expressing a given gene within the cluster. Dot color intensity shows the mean expression level.
(C) Each sample depth in terms of the number of genes.
(D) Each sample depth in terms of the number of unique molecular indices (UMIs).
(E) UMAP plot of cells from the hippocampus.
(F) UMAP plot of cells from the cerebral cortex.

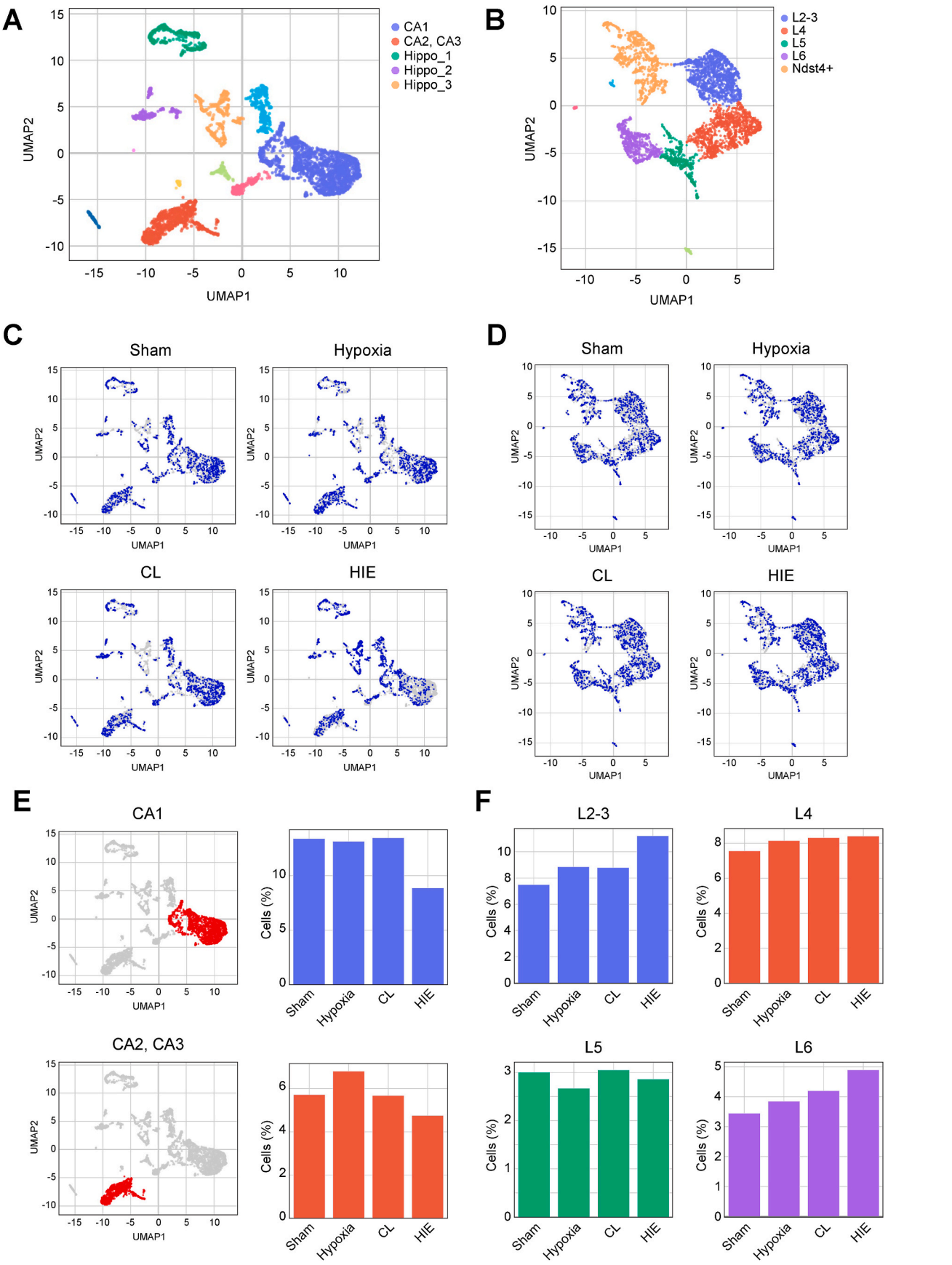

(caption on next page)

Fig. 3. Single-nucleus RNA-seq focused on neurons.
(A) UMAP plot of cells from the hippocampus.
(B) UMAP plot of cells from the cerebral cortex.
(C) Differences in UMAP plots distribution of hippocampus neurons separated into four groups.
(D) Differences in UMAP plots distribution of cerebral cortex neurons separated into four groups.
(E) Difference in the percentage of neurons regarding the CA1-3 region of the hippocampus.
(F) Difference in the percentage of neurons regarding layers of cerebral cortex.

another one that underwent sham surgery alone (sham group). To confirm that our model accurately simulated HIE, we assessed atrophy rates in various brain regions of P14 mice. HE staining revealed significant atrophy, with the ipsilesional hippocampus showing a reduction of approximately 40 % compared to the contralateral side. Milder atrophy (approximately 10 % reduction) was observed across the entire cerebral hemisphere, though minimal differences were noted when focusing solely on the cortex (Fig. 1F, G, H). These findings are consistent with previously reported data [18,19], confirming the robustness of our model.

To generate detailed transcriptomic profiles of HIE model mice, we performed snRNA-seq. Cortical and hippocampal tissues were isolated from four experimental groups: sham (healthy control), hypoxia-only, cerebral ischemia-only, and HIE (combined hypoxia and cerebral ischemia) (see Methods for details). Each group consisted of tissues pooled from four mice (two males and two females). Using the extracted nuclei, we generated sequencing libraries and obtained the following cell counts: 3531, 3571, 3558, and 3595 cortical cells and 3450, 3555, 3526, and 3566 hippocampal cells from the HIE, CL, Hypoxia, and Sham groups, respectively. Visualization of the cell clusters was performed using Uniform Manifold Approximation and Projection (UMAP) (Fig. 2A), which revealed 24 distinct clusters. These clusters were annotated based on the expression of well-established cell type-specific markers (Fig. 2B) [20,21]. The use of snRNA-seq, compared with that of scRNA-seq, enabled us to recover diverse neuronal clusters successfully. A reasonable sequencing depth was achieved for each cell, as evidenced by the number of genes and transcripts detected per cell (Fig. 2C and D). UMAP plots for cells isolated from the hippocampus and cortex (Fig. 2E and F) manifested distinct cell distributions across anatomical locations, confirming the accuracy of tissue collection.

To further investigate phenotypic differences in neurons affected by HIE, we performed sub-clustering analyses focusing on hippocampal neurons (Fig. 3A) and cortical glutamatergic Slc30a3+ neurons (Fig. 3B). In the hippocampus, manual inspection revealed distinct cluster distributions in the HIE group, specifically with neurons corresponding to the CA1 and CA2-3 regions (Fig. 3C). Proportional analysis demonstrated a notable decrease in CA1 neuron proportions in the HIE group compared to other experimental groups (Fig. 3E). Similar studies of cortical neurons showed a less pronounced but observable differential distribution in HIE, highlighting subtler changes compared to those that occurred in the hippocampus (Fig. 3D–F). These results suggest that HIE-induced impairments are highly specific to cell type and anatomical location. Moreover, the combination of hypoxic and ischemic conditions is necessary to induce these region-specific neuronal changes.

Beyond neuronal alterations, we examined microglial responses to HIE. UMAP analysis, segregated by sample, revealed significant shifts in the distribution of hippocampal microglia in response to HIE (Fig. 4A). Although cortical microglial changes were less pronounced, distinct alterations in cell distribution were still evident. Differential expression gene (DEG) analysis was performed by comparing hypoxia, ischemia, and HIE groups to the sham group. The HIE hippocampal samples displayed the highest number of DEGs, followed by the HIE cortical samples (Fig. 4B), while few or no DEGs were detected in other experimental groups. To assess regional differences in gene expression, we generated a heat map comparing DEG profiles from the hippocampus and cortex (Fig. 4C). While DEG patterns shared similarities between these regions, the hippocampus exhibited significantly more pronounced changes. GO analysis of hippocampal DEGs revealed enrichment of genes related to viral response pathways, potentially linked to interferon (IFN) activation (Fig. 4D). This microglial activation in the hippocampus was also validated by ionized calcium-binding adaptor molecule 1 (Iba-1) immunostaining in the ipsilesional hippocampus of the HIE group (Fig. 4E). The HIE group showed a significantly increased percentage of Iba-1 positive area in the ispiletional hippocampus, indicating microglial accumulation (Fig. 4F).

6. Discussion

We employed snRNA-seq to comprehensively analyze the brain damage in a mouse HIE model at the single-cell level. We aimed to understand the underlying mechanisms of HIE better. The generated data provide high-quality insights, revealing that neuronal damage in HIE occurs in a cell type- and region-specific manner. We found that the severity of impairment observed through snRNA-seq closely correlates with histological findings, validating the utility of this technique for studying HIE. Moreover, we demonstrated that microglia, in addition to neurons, exhibit similar changes in response to HIE. Importantly, brain atrophy and gene expression changes were most pronounced in the hippocampus, highlighting the hippocampus' potential as a central target for therapeutic strategies aimed at treating or mitigating the effects of HIE.

Microglia, which are activated at the site of nerve injury, can be broadly classified into two types: inflammation-activated (M1) and anti-inflammatory (M2). The regulation of these microglial activities is influenced by the expression of interferon regulatory factor 7 (IRF7), a key transcription factor involved in the type I IFN response [22], which is modulated by transforming growth factor-β1 (TGFβ1) signaling [23]. IRF7 plays a crucial role in the immune response, and the specific DEGs identified in the hippocampus of the HIE group in our study may be linked to the behavior of microglia that accumulate following brain nerve tissue damage.

This study has few limitations. First, the analysis was conducted at a single time point, restricting our ability to observe the progression or potential recovery of the model, indicating an important area for future investigation. Additionally, incorporating other HIE models in future studies could provide a more comprehensive understanding of the condition. It is also essential to determine whether the findings observed in mice are applicable to human pathology, as differences in species may affect the generalizability of the results. In general, P7 rats [8] and P7-10 mice [5,6,18,19] have been used to model the human newborn stage. A recent study [24] reported that, considering the brain, bones, and life cycle, P3 and P10 mice correspond to 24 gestational weeks and 1 year of age in humans, respectively. In this context, it is important to consider the differences in developmental speed between humans and mice.

Nevertheless, this study demonstrates that snRNA-seq is a valuable tool for capturing detailed pathological changes in the brain, particularly those involving neuronal cells. The integration of snRNA-seq with various therapeutic agents and approaches holds great promise for the development of novel treatments for HIE.

CRediT authorship contribution statement

Nao Wakui: Writing – original draft, Visualization, Investigation, Data curation, Conceptualization. **Takashi Shimbo:** Writing – original draft, Formal analysis, Data curation, Conceptualization. **Morifumi Hanawa:** Methodology. **Tomomi Kitayama:** Investigation, Formal

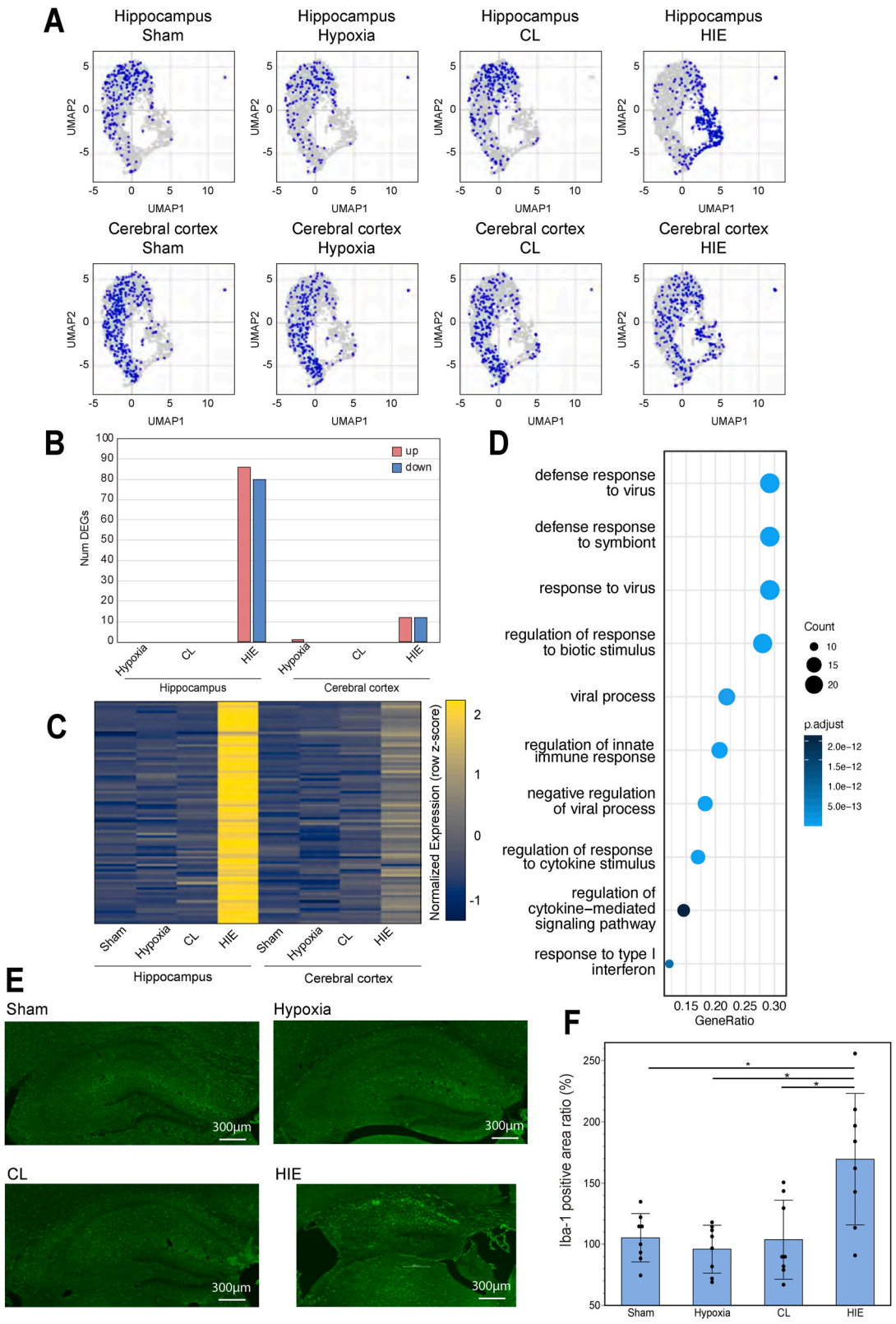

Fig. 4. Single-nucleus RNA-seq focused on microglia.
(A) Differences in UMAP plots distribution of separated hippocampus and cerebral cortex of four groups.
(B) Number of differential expression genes (DEGs) in microglia compared with the Sham group.
(C) Heat map focusing on genes that are upregulated in the hippocampus of the HIE group.
(D) Gene Ontology (GO) analysis on the DEGs from the hippocampus microglia.
(E) Samples of Iba-1 immunostained sections of the ipsilesional hippocampus.
(F) Iba-1 positive area ratio of the hippocampus (ispi/contra). *p < 0.01. Error bars show means + SD. Each group contained four males and four females.

analysis. **Yukari Yamamoto:** Validation, Formal analysis. **Yuya Ouchi:** Visualization, Software, Formal analysis, Data curation. **Kotaro Saga:** Supervision. **Aiko Okada:** Supervision. **Kazuya Mimura:** Supervision. **Katsuto Tamai:** Writing – review & editing, Supervision. **Masayuki Endo:** Supervision, Funding acquisition, Conceptualization.

Data availability

All sequencing data used in this study have been deposited in the Gene Expression Omnius (https://www.ncbi.nlm.nih.gov/geo/; accession number: GSE284245).

Funding sources

This study was funded by StemRIM Institute of Regeneration-Inducing Medicine, Osaka University.

Declaration of competing interest

The authors declare the following financial interests/personal relationships which may be considered as potential competing interests: T. Shimbo and K. Saga received research fundings from StemRIM. T. Shimbo and K. Tamai are StemRIM stockholders. M. Hanawa, T. Kitayama, Y. Ouchi and Y. Yamamoto are employees of StemRIM.

Acknowledgments

We thank Etsuko Ikenoue for the technical assistance.

Appendix. ASupplementary data

Supplementary data to this article can be found online at https://doi.org/10.1016/j.bbrep.2025.102026.

References

[1] Nation institute of neurological disorders and stroke health information-hypoxic ischemic encephalopathy. https://www.ninds.nih.gov/health-information/disorders/hypoxic-ischemic-encephalopathy.
[2] M.D. Douglas-Escobar, M.D. Weiss, Hypoxic-ischemic encephalopathy: a review for the clinician, JAMA Pediatr. 169 (2015) 397–403, https://doi.org/10.1001/jamapediatrics.2014.3269.
[3] B. Li, K. Concepcion, X. Meng, L. Zhang, Brain-immune interactions in perinatal hypoxic-ischemic brain injury, Prog. Neurobiol. 159 (2017) 50–68, https://doi.org/10.1016/j.pneurobio.2017.10.006.
[4] M. Nabetani, T. Mukai, H. Shintaku, Preventing brain damage from hypoxic–ischemic encephalopathy in neonates: update on mesenchymal stromal cells and umbilical cord blood cells, Am, J. Perinatol. 39 (2022) 1754–1763, https://doi.org/10.1055/s-0041-1726451.
[5] E.A. Lemanski, B.A. Collins, A.T. Ebenezer, S. Anilkumar, V.A. Langdon, Q. Zheng, S. Ding, K.R. Franke, J.M. Schwarz, E.C. Wright-Jin, A novel non-invasive murine model of neonatal hypoxic-ischemic encephalopathy demonstrates developmental delay and motor deficits with activation of inflammatory pathways in monocytes, Cells 13 (2024) 1551, https://doi.org/10.3390/cells13181551.
[6] H.R. Chen, C.W. Chen, Y.M. Kuo, B. Chen, I.S. Kuan, H. Huang, J. Lee, N. Anthony, C.Y. Kuan, Y.Y. Sun, Monocytes promote acute neuroinflammation and become pathological microglia in neonatal hypoxic-ischemic brain injury, Theranostics 12 (2022) 512–529, https://doi.org/10.7150/thno.64033.
[7] R. Salomon, D. Kaczorowski, F. Valdes-Mora, R.E. Nordon, A. Neild, N. Farbehi, N. Bartonicek, D. Gallego-Ortega, Droplet-based single cell RNAseq tools: a practical guide, Lab Chip 19 (2019) 1706–1727, https://doi.org/10.1039/c8lc01239c.
[8] J.E. Rice III, R.C. Vannucci, J.B. Brierley, The influence of immaturity on hypoxic-ischemic brain damage in the rat, Ann. Neurol. 9 (1981) 131–141, https://doi.org/10.1002/ana.410090206.
[9] K.B.J. Franklin, G. Paxinos, The Mouse Brain in Stereotaxic Coordinates, Compact, third ed., Academic Press, Mar 18, 2008.
[10] J. Schindelin, I. Arganda-Carreras, E. Frise, V. Kaynig, M. Longair, T. Pietzsch, S. Preibisch, C. Rueden, S. Saalfeld, B. Schmid, J.Y. Tinevez, D.J. White, V. Hartenstein, K. Eliceiri, P. Tomancak, A. Cardona, Fiji: an open-source platform for biological-image analysis, Nat. Methods 9 (2012) 676–682, https://doi.org/10.1038/nmeth.2019.
[11] B.K. Martin, C. Qiu, E. Nichols, M. Phung, R. Green-Gladden, S. Srivatsan, R. Blecher-Gonen, B.J. Beliveau, C. Trapnell, J. Cao, J. Shendure, Optimized single-nucleus transcriptional profiling by combinatorial indexing, Nat. Protoc. 18 (2023) 188–207, https://doi.org/10.1038/s41596-022-00752-0.
[12] J. Cao, J.S. Packer, V. Ramani, D.A. Cusanovich, C. Huynh, R. Daza, X. Qiu, C. Lee, S.N. Furlan, F.J. Steemers, A. Adey, R.H. Waterston, C. Trapnell, J. Shendure, Comprehensive single-cell transcriptional profiling of a multicellular organism, Science 357 (2017) 661–667, https://doi.org/10.1126/science.aam8940.
[13] A. Dobin, C.A. Davis, F. Schlesinger, J. Drenkow, C. Zaleski, S. Jha, P. Batut, M. Chaisson, T.R. Gingeras, STAR: ultrafast universal RNA-seq aligner, Bioinformatics 29 (2013) 15–21, https://doi.org/10.1093/bioinformatics/bts635.
[14] Y. Hao, S. Hao, E. Andersen-Nissen, W.M. Mauck III, S. Zheng, A. Butler, M.J. Lee, A.J. Wilk, C. Darby, M. Zagar, P. Hoffman, M. Stoeckius, E. Papalexi, E.P. Mimitou, J. Jain, A. Srivastava, T. Stuart, L.B. Fleming, B. Yeung, A.J. Rogers, J.M. McElrath, C.A. Blish, R. Gottardo, P. Smibert, R. Satija, Integrated analysis of multimodal single-cell data. bioRxiv, 2020, https://doi.org/10.1101/2020.10.12.335331.
[15] G. Yu, L.G. Wang, Y. Han, Q.Y. He, clusterProfiler: an R Package for Comparing Biological Themes Among Gene Clusters, vol. 16, Omics, 2012, pp. 284–287, https://doi.org/10.1089/omi.2011.0118.
[16] T. Wu, E. Hu, S. Xu, M. Chen, P. Guo, Z. Dai, T. Feng, L. Zhou, W. Tang, L. Zhan, X. Fu, S. Liu, X. Bo, G. Yu, clusterProfiler 4.0: a universal enrichment tool for interpreting omics data, Innovation (Camb.) 2 (2021) 100141, https://doi.org/10.1016/j.xinn.2021.100141.
[17] E. Guangchuang Yu, Bioconductor. https://www.bioconductor.org/packages/release/bioc/html/enrichplot.html, 2023.
[18] K.E. Hawkins, M. Corcelli, K. Dowding, A.M. Ranzoni, F. Vlahova, K.L. Hau, A. Hunjan, D. Peebles, P. Gressens, H. Hagberg, P. de Coppi, M. Hristova, P. V. Guillot, Embryonic stem cell-derived mesenchymal stem cells (MSCs) have a superior neuroprotective capacity over fetal MSCs in the hypoxic-ischemic mouse brain, Stem Cells Transl. Med. 7 (2018) 439–449, https://doi.org/10.1002/sctm.17-0260.
[19] R. Zen, T. Terashima, S. Tsuji, M. Katagi, N. Ohashi, Y. Nobuta, A. Higuchi, H. Kanai, T. Murakami, H. Kojima, Ambient temperature is correlated with the severity of neonatal hypoxic-ischemic brain injury via microglial accumulation in mice, Front. Pediatr. 10 (2022) 883556, https://doi.org/10.3389/fped.2022.883556.
[20] Z. Yao, C.T.J. van Velthoven, T.N. Nguyen, J. Goldy, A.E. Sedeno-Cortes, F. Baftizadeh, D. Bertagnolli, T. Casper, M. Chiang, K. Crichton, S.L. Ding, O. Fong, E. Garren, A. Glandon, N.W. Gouwens, J. Gray, L.T. Graybuck, M.J. Hawrylycz, D. Hirschstein, M. Kroll, K. Lathia, C. Lee, B. Levi, D. McMillen, S. Mok, T. Pham, Q. Ren, C. Rimorin, N. Shapovalova, J. Sulc, S.M. Sunkin, M. Tieu, A. Torkelson, H. Tung, K. Ward, N. Dee, K.A. Smith, B. Tasic, H. Zeng, A taxonomy of transcriptomic cell types across the isocortex and hippocampal formation, Cell 184 (2021) 3222–3241.e26, https://doi.org/10.1016/j.cell.2021.04.021.
[21] B. Tasic, Z. Yao, L.T. Graybuck, K.A. Smith, T.N. Nguyen, D. Bertagnolli, J. Goldy, E. Garren, M.N. Economo, S. Viswanathan, O. Penn, T. Bakken, V. Menon, J. Miller, O. Fong, K.E. Hirokawa, K. Lathia, C. Rimorin, M. Tieu, R. Larsen, T. Casper, E. Barkan, M. Kroll, S. Parry, N.V. Shapovalova, D. Hirschstein, J. Pendergraft, H. A. Sullivan, T.K. Kim, A. Szafer, N. Dee, P. Groblewski, I. Wickersham, A. Cetin, J. A. Harris, B.P. Levi, S.M. Sunkin, L. Madisen, T.L. Daigle, L. Looger, A. Bernard, J. Phillips, E. Lein, M. Hawrylycz, K. Svoboda, A.R. Jones, C. Koch, H. Zeng, Shared and distinct transcriptomic cell types across neocortical areas, Nature 563 (2018) 72–78, https://doi.org/10.1038/s41586-018-0654-5.
[22] K. Honda, H. Yanai, H. Negishi, M. Asagiri, M. Sato, T. Mizutani, N. Shimada, Y. Ohba, A. Takaoka, N. Yoshida, T. Taniguchi, IRF-7 is the master regulator of type-I interferon-dependent immune responses, Nature 434 (2005) 772–777, https://doi.org/10.1038/nature03464.
[23] M. Cohen, O. Matcovitch, E. David, Z. Barnett-Itzhaki, H. Keren-Shaul, R. Blecher-Gonen, D.A. Jaitin, A. Sica, I. Amit, M. Schwartz, Chronic exposure to TGFβ1 regulates myeloid cell inflammatory response in an IRF7-dependent manner, EMBO J. 33 (2014) 2906–2921, https://doi.org/10.15252/embj.201489293.
[24] N.C. Cottam, K. Ofori, K.T. Stoll, M. Bryant, J.R. Rogge, K. Hekmatyar, J. Sun, C. J. Charvet, From circuits to lifespan: translating mouse and human timelines with neuroimaging-based tractography, J. Neurosci. 45 (2025) e1429242025, https://doi.org/10.1523/JNEUROSCI.1429-24.2025.